Coarse-grained molecular dynamics investigation of nanostructures and thermal properties of porous anode for solid oxide fuel cell

Yan-Feng Wang [a,b,*], Jinliang Yuan [a], Bengt Sundén [a], Yu-Li Hu [b]

[a] Department of Energy Sciences, Faculty of Engineering, Lund University, Box 118, SE-221 00 Lund, Sweden
[b] School of Marine Science and Technology, Northwestern Polytechnical University, Xi'an 710072, PR China

HIGHLIGHTS

- An AA-CG-MD method is developed to simulate the fabrication process of the porous anode of SOFC.
- This method is employed to reconstruct the microstructure of the porous anode vividly.
- Relevant thermal properties are calculated in a rapid and accurate manner on the basis of the method.
- Analyses and predictions are proceeded to capture the good performance for the porous anode of SOFC.

ARTICLE INFO

ABSTRACT

Incorporation of nanoscale catalysts into porous structures of SOFC has been proven highly successful in increasing active sites and catalyst utilization. In addition, electrochemical reactions as well as heat transfer process in porous anode are strongly affected by complex porous structures. It is believed that study of anode thermal properties are critical for SOFC design and operation. In this work, an AA model is developed for nickel and YSZ components via ASE, and a CG technique is further applied to represent Ni and YSZ beads by VMD, which are then self-assembled to capture the anode nanostructure via GRO-MACS. LAMMPS is then employed to evaluate average thermal properties of the porous anode. It is found that, at low Ni content ($\leq$30 vol%), thermal conductivity increases with increasing temperature due to lattice vibrations. Instead, the anode exhibits metallic behavior due to rich nickel phase. Thermal expansion of the anode increases with increasing nickel content. Average thermal properties of the anode are validated by open literature data with good agreement. This approach is considered to be applied to analyze nanostructures, heat transfer and temperature distribution in the porous anode, and is also useful to capture thermal performance of SOFC and stack.

© 2014 Elsevier B.V. All rights reserved.

1. Introduction

Solid oxide fuel cell (SOFC) is an attracting energy-converting device due to its high energy efficiency [1,2] and fuel flexibility [3,4], as well as low pollutant emissions [5]. SOFC employs multi-layered electrodes which comprise ceramic and metallic materials with different thermal properties. All components, e.g., anode, cathode, electrolyte, etc., have to provide a well-adjusted heat diffusion, thermal expansion, mechanical strength and so on, both at material interfaces and inside materials. The performance of SOFC is not only determined by intrinsic material properties, but also subject to the fabrication technology of functional layers. Basically, that can be improved by the application of modified materials using appropriate technologies. It is well known that the higher operating temperatures in SOFC improve its performance in comparison with low-temperature fuel cells, e.g., PEMFC, DMFC, PAFC, etc. In addition, high operating temperatures make it feasible to carry out electrochemical reactions in the active sites of the porous anode with cheap catalysts. On the other hand, the internal reforming reactions of hydrocarbon fuels, e.g., methane, are contributing to keep a good balance of heat generation and consumption. Heat is mainly produced in the exothermically electro-chemical reactions. However, it is noticed that too much cooling caused by the endothermic steam reforming reactions has a negative effect on the output performance of SOFC [6], which is remarkably opposed to desired thermal management in the porous anode for SOFC. Thus, studying heat transfer in order to effectively

---

* Corresponding author. Department of Energy Sciences, Faculty of Engineering, Lund University, Box 118, SE-221 00 Lund, Sweden. Tel.: +46 46 222 9439; fax: +46 46 222 4717.
E-mail address: Yanfeng.Wang@energy.lth.se (Y.-F. Wang).

enhance the thermal management inside the porous anode has been attracting significant attention in the recent years. This means that to correctly predict the thermal properties of the porous anode of SOFC is important in developing high-performance SOFCs.

In order to generate high power density and achieve reaction-related efficiency as high as possible, abundant triple-phase boundaries (TPBs) [7,8], where the electrochemical reactions take place, should be available in the porous electrodes. This explicitly represents a principle that to sinter high porosity in the functional anode seems extremely important for the extensive distribution of so-called TPBs. Unfortunately, for the well-dispersed porous anode from nanoscale particles, e.g., Ni and yttria-stabilized zirconia (YSZ) [9,10], etc., significant reduction of the thermal conductivity is expected due to discontinuities inside mediated materials, which is described adequately by effective medium theory (EMT) [11]. The mechanical strength of the porous anode is also prone to be lowered to a certain extent. It is thus extremely important to keep a good balance among high porosity, considerable thermal diffusion and acceptable mechanical strength in the porous anode of SOFC. In addition, high temperature gradients will easily take place along and normal to the direction of fuel flow due to mass diffusion or concentration drop of the fuel gas. This will be mainly attributed to the unreasonable cooling effect due to the high supply rate of the air flow in the cathode. It is found that a sharp temperature gradient or thermal stress is primarily responsible for cracking in the porous anode, even in the electrolyte. The temperature gradient or the thermal stress accounted for by heat transfer inside the SOFC can be computed numerically but really depends on specific heat capacity as well as heat flow rate and thermal conductivity (TC), etc.

In this work, an all-atom coarse-grained molecular dynamics (also named AA-CG-MD) method is employed. In brief, a target domain with cubic 50 nm (typically limited by GROMACS, the code used to reconstruct the nanostructures of the porous anode, especially the TPB region) will be implemented from the ab initio stage, e.g., atoms, molecules, lattices, etc. The box will be filled with beads, also named "pseudo atoms", representing groups of atoms/molecules to be computed in the MD approach. The model may be developed for the reforming and electrochemical reactions, mass and charge transfer, and heat diffusion. The predicted material properties in this study based on the open literature data [12—16] are linked to the compositions and nanostructures of the materials. Some basic principles govern the choices of SOFC materials. For example, the electrodes should have high electrical conductivity for the charge transport, high catalytic activity for the involved reforming and electrochemical reactions, adequate porosity for the gas/vapor diffusion, good physical/chemical compatibility with the electrolyte and interconnect for the long-term stability.

As experimental measurements tend to be more costly and difficult to carry out compared with the simulation work, which is speedy and relatively easy once the model is programmed and validated, their ability to investigate the effects of different material parameters and operating conditions on the performance of SOFC is critically limited. Numerical modeling and simulations incorporating the known physical and chemical phenomena occurring inside SOFC to predict its performance are quite important for the understanding and technological improvement of SOFC. Though there is no shortage of research on the numerical modeling for SOFC, the analysis focusing on the effects of nanostructures in the porous anode on thermal properties is relatively rare in the open literature. Therefore, it seems that such a research effort is quite essential for improving the performance of SOFC. In this case, the thermal properties, electrochemical performance and their interplay are supposed to be taken into account to properly extract the best performance for SOFC to practical applications. This work

describes a detailed nanoscale model for the numerical simulations in the porous anode of SOFC with a representative Ni/YSZ—YSZ—LSM/YSZ setup [17,18]. The thermal properties of the porous anode are determined and evaluated against the open literature data [19—22]. Anodic nanostructure, as well as effects of Ni contents, and sintering conditions of the anode on its thermal properties are systematically investigated. Finally, the desired material compositions and anodic nanostructures are deduced.

2. Modeling development

In this study, the AA-CG-MD approach is firstly implemented to reconstruct microscopic structures for the porous anodes at the nanoscale, and the obtained structures are further applied to calculate thermal properties of the porous anodes, e.g., average TC, thermal expansion coefficient (TEC), volumetric heat capacity (VHC), etc. The size effect on TC is also evaluated. These contribute to further predict the probability of thermal failure and evaluate the overall performance of the porous anode of SOFC [23—25] by the MD modeling [26]. The precise details of the method are presented in the following three steps.

2.1. All-atom modeling

In classical MD modeling, a single potential energy surface is represented in the force-field, which is a consequence of Born—Oppenheimer (BO) approximation [27,28]. Therefore, it is possible to compute the wave-function and the energy of an atom/molecule in finite and less complicated steps.

$$\Psi_{\text{total}} = \chi_{\text{electronic}} \times \phi_{\text{nuclear}} \qquad (1)$$

where Ψ referring to Equation (1), allows the wave-function of an atom/molecule to be broken into its electronic and nuclear components.

In excited states, when electrochemical reactions or a more accurate representation are needed, electronic behavior can be obtained from first principles [29] by using a quantum mechanical method, such as Density Functional Theory (DFT) [9,20]. This is known as the AA modeling [30]. Due to treating electronic degrees of freedom, the computational cost of this method is much higher than classical MD, which implies that the AA modeling is limited to smaller systems and shorter periods of time. In general, this modeling is usually made in the close neighborhood of the atom/molecule-based systems. Although various approximations may be used, these are based on theoretical considerations instead of empirical fitting. The AA calculations generate a huge amount of information that is not available from empirical methods, such as density of electronic states or other electronic properties. A significant advantage of using the AA modeling is the ability to study nanostructures, even interactions that involve breaking or formation of covalent bonds, which correspond to multiple electronic states and potential energy. In this study, the AA modeling is mainly applied to generate the nanocrystals for sintering powders at the atom-scale, i.e., Ni and YSZ particles. The face-centered cubic (FCC) nickel nanocrystals are generated according to the AA modeling, and partially stabilized tetragonal YSZ nanocrystals are also produced very well by the same technique, and then both of them compose the so-called "green body" (GB) [31] for sintering the porous anodes. Although no open literature data supports that the crystalline nanostructure shows higher oxygen-ion conductivity than the amorphous nanostructure in the porous anode, extensive research work has been focused on this over the past decades. It has been found that the crystalline nanostructure is more stable energetically compared to the amorphous nanostructure in the porous

anode [32]. For these smaller systems, the AA modeling re-constructs the crystalline nanostructures of the sintering particles for the porous anode in excellent agreement with SEM/TEM [22,33] patterns, and to some extent, for much larger systems, this approach can still reveal the approximate morphological occupancy for Ni/YSZ composition, although the interactions of Ni/YSZ particles become poorly determined.

2.2. Coarse-graining modeling

On the other end of nanoscale, there are coarse-grained and lattice models. Instead of explicitly representing every atom/molecule of the system, one uses "pseudo-atoms" to represent groups of atoms. Further speaking, CG [34,35] is composed of replacing an atomic description of an atom/molecule with a lower-resolution coarse-grained particle that averages or smoothes away fine details.

The MD simulations on very large systems may require such huge computing resources that they cannot easily be studied by the traditional AA modeling. Similarly, simulations at long time-scales (typically more than 1 μs) are prohibitively expensive, because they require so many time-steps. In these cases, one can sometimes handle the problem by using reduced or simplified representations, also named the coarse-grained (CG) models, which have been developed to investigate many complex systems, e.g., lipid mem-branes, proteins, ceramics, etc., at the longer time/length-scales. The following formula calculates the system's potential energy as a sum of individual energy terms when the CG representation is implemented.

$$V(r_{ij}) = V_{bonded}(r_{ij}) + V_{nonbonded}(r_{ij}) \qquad (2)$$

where the components of the bonded/nonbonded contributions are specified by the following equations, as outlined separately in Equations (3) and (7).

$$V_{bonded}(r_{ij}) = V_{bond}(r_{ij}) + V_{angle}(\theta_{ijk}) + V_{dihedral}(\varphi_{ijkl}) \qquad (3)$$

in which,

$$V_{bond}(r_{ij}) = \sum_{pairs} \frac{1}{2} K_{ij}^b (r_{ij} - b_{ij}^0)^2 \qquad (4)$$

$$V_{angle}(\theta_{ijk}) = \sum_{angles} \frac{1}{2} K_{ijk}^\theta (\theta_{ijk} - \theta_{ijk}^0)^2 \qquad (5)$$

$$V_{dihedral}(\varphi_{ijkl}) = \sum_{dihedrals} K_{ijkl}^\varphi [1 + \cos(n\varphi_{ijkl} - \varphi_{ijkl}^0)] \qquad (6)$$

where r_{ij} is the distance between bead i and bead j; θ_{ijk} is the angle among beads i, j and k; φ_{ijkl} is the proper dihedral among surface ijk and surface jkl; K represents the force constant; b^0, θ^0 and φ^0 are critical values. In this work, the bond and angle terms are modeled as harmonic potentials centered equilibrium bond-length values. Empirically, the force constants of K_{bond}, K_{angle} are specified as 1250 kJ mol^{-1} nm^{-2}, 25 kJ mol^{-1} rad^{-2} [35], respectively. The involved critical values are determined by shape-based coarse-graining (SBCG) tool of Visual Molecular Dynamics (VMD) package when the nanostructure transforming is implemented from the AA representation to the CG beads.

In contrast with the bonded terms, it is much more computa-tionally costly to calculate the nonbonded terms because a given bead is bonded to only a few of its neighbors, but interacts with every other bead in the target system.

$$V_{nonbonded}(r_{ij}) = V_{vanderWaals}(r_{ij}) + V_{electrostatic} \qquad (7)$$

As one of the nonbonded interactions, the van der Waals term falls off rapidly with distance. It is typically modeled as the Lennard-Jones form, as treated also in this study.

$$V_{LJ}(r_{ij}) = \sum 4\varepsilon_{ij} \left[\left(\frac{\sigma_{ij}}{r_{ij}}\right)^{12} - \left(\frac{\sigma_{ij}}{r_{ij}}\right)^6 \right] \qquad (8)$$

where ε_{ij} is the depth of the potential well; σ_{ij} is the finite distance at which the inter-particle potential is zero, and a cut-off radius of 0.43 nm [35] is employed simultaneously in this study.

In addition, the Coulomb form is used to address the electro-static term of the nonbonded interactions in Equation (7).

$$V_{Coulomb}(r_{ij}) = \sum \frac{1}{4\pi\varepsilon_0} \frac{q_i q_j}{r_{ij}} \qquad (9)$$

where q_i and q_j are the charges of the particles i and j, respectively; ε_0 is the electric permittivity (8.85E-12 F m^{-1}).

It is remarkably worth noting that those coarse-grained systems are in fact limited by the dynamical accuracy and structure-based properties. The research work relevant to CG is in its infancy, and its theoretical fundamental basis is still poorly understood. How-ever, CG has already been widely employed in the area of MD.

In this section, as sintering powders, the nanocrystals of Ni and YSZ generated by the above AA modeling are represented by a few "pseudo-atoms" which gather around 50 Ni or YSZ atoms/mole-cules into each "pseudo-atom". Subsequently, the virtual bonded/non-bonded interactions taking place among the "pseudo-atoms", e.g., bonds, angles, torsion, van der Waals interactions, etc., are extracted as well via the CG builder (one module of VMD package), by which the CG-MD force-field is in principle achieved. Unfortu-nately, the parameterized process for CG must be conducted really dependent on experience, by matching the behavior of the modeling to appropriate open-source data obtained by the exper-iments or numerical computations. Ideally, these parameters should account for both bonded and non-bonded contributions to potential energy in an explicit way. Sometimes, when CG is done at higher levels, the accuracy of the dynamic description may be less reliable relatively. But a few coarse-grained models have been used successfully to tackle a wide range of problems in structure-based research work.

2.3. AA-CG-MD modeling

In general, MD is a numerical simulation method for the phys-ical/chemical phenomena in complex systems, which may involve thermal management, mass and charge transport, together with internal reforming reactions and electrochemical reactions in the porous anode of SOFC. The particles (i.e., atoms, molecules, even "pseudo atoms") from the large systems are allowed to interact within a period of time, and then give a view of the motion of the computed particles. Theoretically, these are determined by numerically solving the Newton's equation of motion for a system of interacting particles, as below.

$$\vec{F_i} = m_i \frac{\partial^2 \vec{r_i}}{\partial t^2} = -\frac{\partial V(r_{ij})}{\partial \vec{r_i}} \qquad (10)$$

where m_i is the mass of the particle i, $\vec{r_i}$ is the position of the particle, $V(r_{ij})$ is the potential energy.

The forces among the particles and the potential energy (typi-cally including bond, angle, dihedral, improper dihedral, van der

Waals and electrostatic potentials), are determined by the prebuilt MD force-fields, e.g., MARTINI [36] (a coarse-grained force-field developed by Marrink and coworkers at the University of Groningen), GROMACS [37,38] (the force-field optimized for GROMACS), VAMM (Virtual atom molecular mechanics), etc. Basically, it is almost impossible to obtain all properties of such complex systems in an analytical way due to the large amount of particles involved. Fortunately, the MD simulation appears to circumvent perfectly this limitation by utilizing numerical approaches, if it is ignored that to run long MD simulations appears ill-conditioned in mathematics. This phenomenon is mainly attributed to cumulative errors during integrations, which can be inhibited slightly with suitable parameters and algorithms implemented, but not eliminated entirely. Despite the theoretical support behind the MD modeling is still insufficient, extensive research work has been focused on achieving macroscopic thermodynamical properties of the target system, e.g., TC, VHC, TEC, etc., in terms of ergodic hypothesis (EH) [39,40] that the statistical ensemble average is equivalent to the time average on the simulated system.

In this part, on the basis of the above AA modeling and CG representations, not only are nanostructures of the porous anode of SOFC reconstructed via GROMACS, but also thermal properties (including TC, VHC, and TEC) and size effect of the porous anode are numerically calculated through Large-scale Atomic/Molecular Massively Parallel Simulator (LAMMPS) package, an acronym for LAMMPS. In addition, the combined AA-CG-MD method is developed in detail and validated by comparing the prediction results with the open literature data, and it is also providing some insight into an interconnection of sintering conditions of GB involving Ni and YSZ nanocrystals, the nanostructures of the porous anode in morphology and the resulted thermal properties of the porous anode at the nanoscale.

2.4. Numerical solution method

In this work, a numerical solution method is developed to reconstruct and evaluate the porous anode based on the above three aspects. First, NiO/YSZ nanocrystals are built at atomic level using Atomistic Simulation Environment (ASE) package, which provides PYTHON modules for manipulating atoms and determining interactions of atoms in terms of DFT. When the atomic numbers and lattice constants are specified, the DFT calculations of NiO/YSZ nanocrystals are performed by the Jacapo calculator, which is an ASE interface for Dacapo and fully compatible with ASE package. In the Jacapo, the ultra-soft pseudopotentials are used to describe the interactions between valence and core electron, and the wave-functions are expanded in plane waves with the kinetic energy cutoff of 350 eV. To describe electron exchange–correlation interactions, one adopted a generalized gradient approximation with the Perdew–Wang function [41]. Thus, the crystalline structure of NiO/YSZ nanocrystals can be created accurately without information lost. In result, the NiO nanocrystal is modeled by 125 FCC lattices, and each NiO lattice has two nested FCC lattices of nickel and oxygen. Similarly, the YSZ nanocrystal is also built by 125 tetragonal lattices. Secondly, NiO/YSZ nanocrystals are coarse-grained from atom representation to groups of atoms (beads) by VMD package to reduce degrees of freedom and improve the computational efficiency. Meanwhile, interactions of the beads are also established using the SBCG module of VMD package. Neighboring beads are connected by harmonic springs, while separate molecules interact through nonbonded forces. Interactions are parameterized on the basis of the AA model and available experimental data. Therefore, there are around 6 NiO/YSZ lattices in one bead of the NiO/YSZ nanocrystal. By this method, the typical NiO/YSZ nanocrystal with the size of $5 \times 5 \times 5$ lattices is represented by

20 nonpolar beads, respectively. Thirdly, a target box with cubic 50 nm representing the interface region between Ni/NiO and YSZ phases is generated in GROMACS package, and then 26,260 NiO beads and 20,000 YSZ beads are randomly dispersed into the target box. The energy minimization is performed in the course of a step integration procedure to find a local potential energy minimum near the starting structure. This short energy minimization looses the overlapped beads at the beginning. MD running is following energy minimization, which usually includes compressing, heating and equilibrating the system, respectively. In addition, it is often advisable to perform equilibration using weak-coupling techniques for temperature and pressure, especially if the system is far from equilibration. The Berendsen algorithm is applied here to control the system pressure and temperature. The equilibrating process is conducted subsequently for around 200 ns in a canonical (NTV) ensemble. During the simulation, the results and data are auto-saved every 1000 steps (10 ns) and used for later analysis. In result, the nanostructure of the anode is reconstructed after the MD running. Based on the anodic nanostructure, thermal properties can be evaluated systematically using LAMMPS package. In this study, all simulations are programmed in the command-line interface from GROMACS and LAMMPS package. However, there is a format transformation from GROMACS data to an input file of LAMMPS, which is implemented using MATLAB code.

3. Results and discussion

In general, a solid oxide fuel cell is composed of four functional layers, i.e., anode, electrolyte, cathode and interconnect. The first three of these are YSZ ceramic-based. In this work, a popular setup of Ni/YSZ–YSZ–LSM/YSZ is employed. It should be noted that the ion conductivity in YSZ is strongly dependent on the operating temperature. Consequently, SOFC has to be operated at appropriate temperatures ranging from 800 K to 1200 K. Heat transfer process has been focused on in particular, which always takes place along with internal reforming reactions in the porous anode for hydrocarbons, e.g., methane, ethane, ethanol, etc., and electrochemical reactions, typically involving oxidations of H_2/CO in the porous anode and reduction of O_2 in the porous cathode. On the one hand, as a feedstock for SOFC, mainly including H_2, CO, and CH_4, they must be heated to a certain temperature, in which CH_4 is internally reformed into H_2/CO with heat energy consumed due to the endothermic steam reforming reaction. On the other hand, reduction of oxygen into oxygen ions takes place in the cathode with heat energy released due to the exothermic reaction, and then the oxygen ions are transported through the electrolyte to the anode where they can electrochemically oxidize H_2/CO with heat released owing to the exothermic reactions. In addition, electric resistance of the materials also accounts for the heat production as a result of Joule Effect (JE). In other words, heat production and consumption occurring in SOFC, especially in the anode, must be managed dynamically, because heat transfer can either have an effect on the comprehensive efficiency of SOFC, or probably result in thermal failure. Therefore, when heat transfer process inside SOFC is mentioned, some remarkable parameters must be taken into account, as highlighted in the following sessions.

3.1. Nanostructure

To investigate effects on the functional components of SOFC anodes, the sintering processes and nanocrystalline structures have been studied extensively over the past decades. In fabrication processes, the porous anode is multilayered co-sintered in order to obtain better densification and dispersity. Actually, this

manufacturing process can be simulated very well by using the AA-CG-MD method, which totally mimics the crystallization of the NiO/YSZ nanoparticles and the self-assembly phenomena of above particles taking place in the sintering process. This is quite inspiring for exploring the comprehensive performance of the porous anode via the numerical method instead of the expensive and complicated experiments. In this work, a small domain (see Fig. 1) with cubic 50 nm is selected from all interface regions between Ni and YSZ clusters, which is corresponding to TPB features, as shown in Fig. 2, and then the MD simulation is implemented in the thermostat and barostat conditions, respectively, until the simulation system achieves the equilibration that all components of the porous anode can be expressed with balanced porosity, connectivity, dispersity and tortuosity. In the simulation process, the Berendsen weak coupling method is applied in regulating the temperature and pressure of the system based on initially isotropic temperature and pressure. Because at the nanoscale, atomic or molecular motion is dynamic and disordered, therefore, it is assumed that thermal properties relevant to the porous anode in this study are isotropic. In addition, a comparison of the MD-based nanostructure and the TEM-based image of the porous anode is discussed as follows.

Fig. 1 shows numerical reconstruction of the porous anode obtained through the AA-CG-MD method using GROMACS package, mimicking the experimental fabrication process. First, the NiO and YSZ anodic nanocrystals are generated as the sintering powders, including $5 \times 5 \times 5$ NiO lattices consistent with the experimental result as highlighted in Fig. 2 and $5 \times 5 \times 5$ YSZ lattices, using ASE package, which provides PYTHON-based modules for building and manipulating atoms, analyzing simulations, visualizations, etc., at the atom level. Secondly, the NiO and YSZ nanocrystals are coarse-grained into "pseudo particles" (beads), representing groups of atoms by VMD package, which supplies a SBCG tool for transforming nanostructures from AA representation to CG beads. According to a neural network learning algorithm, the SBCG approach is employed to determine placements and
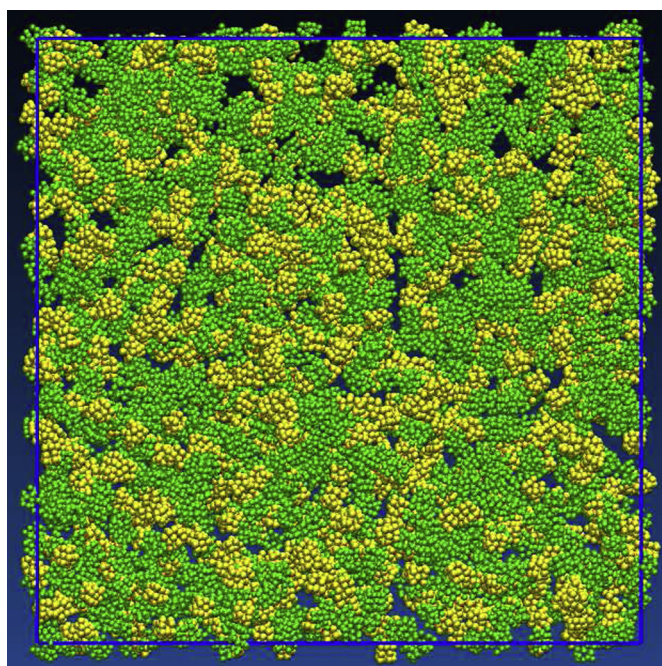

Fig. 2. The TEM-based image of the porous anode of SOFC, in which the white color represents pores (gas phase), the silver color NiO/Ni phases, and the gray color YSZ phase [20].

interactions of all CG beads, and also to attach correct mass to each bead. Thirdly, 26,260 NiO beads and 20,000 YSZ beads in total are randomly dispersed into the $50 \times 50 \times 50$ nm^3 simulation box, and then a MD running is conducted over 20 ns using GROMACS package. After the MD running, the final structure configuration is obtained for the equilibrium state as shown in Fig. 1. In view of the XY plane, an even self-assembly phenomenon is exhibited. The NiO beads in green agglomerate together and compose the NiO phase for conducting electrons. The YSZ beads in yellow are connected to transport oxygen ions. Pores are also dispersed evenly for diffusing gas and water. In addition, all three phases are linked, as expected, to provide the active sites where the electrochemical reaction takes place. Figs. 1 and 2 show the common morphology of the porous anode of SOFC, which is basically dependent on the sintering technology. Meanwhile, Fig. 1 displays more detailed nanostructure of TPB regions in the porous anode and the self-assembly phenomenon compared to Fig. 2 [20]. In the beginning, the NiO phase exists inside the anode, when the electrochemical reactions start, the NiO phase will be reduced into the Ni phase in the hydrogen atmosphere. In fact, the Ni phase instead of NiO phase is functional for conducting electrons and catalyzing the reactions in the operating process of SOFC. When the electrochemical reactions end, the Ni phase will be oxidized into the NiO phase again. So the Ni and NiO phases co-exist in the porous anode, and the redox process between them circulates. In addition, each phase must be continuous as much as possible in order to conduct charges (oxygen-ions and electrons) and diffuse gases (H$_2$/CO and vapor). Meanwhile, all phases must be dispersed as much as possible because abundant TPBs are needed for electrochemical reactions taking place at a high rate. According to Fig. 1, it is easily found that the nano-sintering technology contributes to make the functional components dispersed very well, which is quite meaningful for increasing the TPB's length. In other words, the self-assembly phenomena take place at the nanoscale, inspiringly, by which the continuity, dispersity and porosity are balanced very well to some extent.

Fig. 1. The nanostructure of the porous anode of SOFC with cubic 50 nm, in which the green color represents NiO phase, the yellow color YSZ phase, and the pores gas phase. (For interpretation of the references to color in this figure legend, the reader is referred to the web version of this article.)
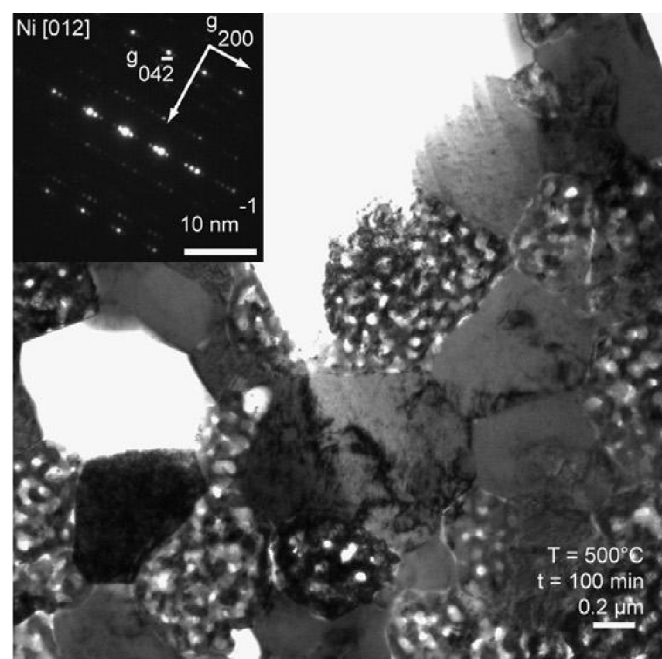
3.2. Thermal conductivity

Heat conduction always happens within or through a body by microscopic diffusion and collisions of involved particles, e.g., electrons, atoms, molecules and phonons, etc., due to a temperature gradient. In this study, the porous anode is totally made up of NiO and YSZ species in the form of CG particles. As a result, heat conduction is mediated by the combination of vibrations and collisions of adjacent free electrons, and of propagation, collisions and scattering of phonons. TC is an inherent property of thermal-conductive materials, which is basically temperature-dependent and commonly included in Fourier's law for heat conduction, presenting that the local heat flux is proportional to the negative temperature gradient as follows.

$$\overrightarrow{q} = -k\nabla T \tag{11}$$

So in this case it seems quite essential to estimate TC of the anode of SOFC. For the engineering fabrication of the cermet-based anode, a multi-layered [42,43] co-sintering [44,45] technique is traditionally employed to create the porous and multi-layered anode from NiO and YSZ powders, which is always implemented at high temperatures but below the melting points of the used materials. This is so because at higher temperatures, phase transformation for YSZ component occurs from the monoclinic crystal phase to the tetragonal crystal phase. The tetragonal phase for YSZ nanocrystals contributes to eliminate the potential crack in the porous anode, which is prone to take place due to unmatched thermal expansion between Ni and YSZ materials. In principle, appropriately high pressures are also applied at the initial stage for sintering in order to pursue the multi-layered anode with suitable porosities [46,47], normally around 30–40 vol%. In these cases, TC is numerically calculated for the porous anodes reconstructed at various pressures ranging from 5 bar to 10 bar and at a certain temperature of 1600 K according to an equilibrium MD approach, i.e., the Green–Kubo (GK) method [19,48,49]. In this method, the average TC in the porous anodes is related to the ensemble average of the auto-correlation of the heat flux into or out of the computing domain and a universal temperature.

$$\mathbf{J} = \frac{1}{V}\left[\sum_i e_i\mathbf{V}_i - \sum_i \mathbf{S}_i\mathbf{V}_i\right]$$
$$= \frac{1}{V}\left[\sum_i e_i\mathbf{V}_i + \sum_{i<j}\left(\mathbf{f}_{ij}\cdot\mathbf{V}_j\right)\mathbf{X}_{ij}\right] \tag{12}$$
$$= \frac{1}{V}\left[\sum_i e_i\mathbf{V}_i + \frac{1}{2}\sum_{i<j}\left(\mathbf{f}_{ij}\cdot(\mathbf{V}_i+\mathbf{V}_j)\right)\mathbf{X}_{ij}\right]$$

$$k = \frac{V}{k_B T^2}\int_0^\infty \langle J_x(0)J_x(t)\rangle dt = \frac{V}{3k_B T^2}\int_0^\infty \langle \mathbf{J}(0)\cdot\mathbf{J}(t)\rangle dt \tag{13}$$

where $\mathbf{J}$ is the heat flux, e_i is the per-atom energy, including potential and kinetic energy, S_i is the per-atom stress tensor, $\mathbf{V}_i$ is a matrix-vector multiply.

As shown in Fig. 3, TC of the porous anodes with the composition of $Ni_{0.33}YSZ$ is slightly proportional to measuring temperatures, which is accounted for by phonon heat conduction. Theoretically, TC involved in phonons is usually described by the Boltzmann equation [34,50,51], in which TC is positively related to measuring temperature.
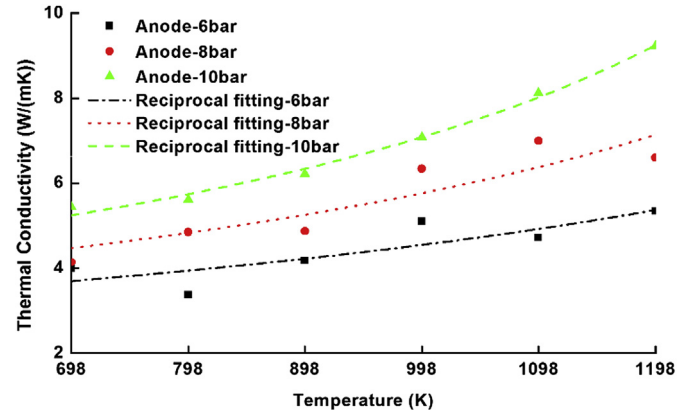

Fig. 3. TC of the porous anodes with $Ni_{0.33}YSZ$ reconstructed at various pressures and 1600 K.

$$\frac{d\langle n\rangle}{dt} = \left(\frac{\partial\langle n\rangle}{\partial t}\right)_{\text{diffusion}} + \left(\frac{\partial\langle n\rangle}{\partial t}\right)_{\text{decay}} \tag{14}$$

$$\left(\frac{\partial\langle n\rangle}{\partial t}\right)_{\text{diffusion}} = -v_x\frac{\partial\langle n\rangle^0}{\partial T}\frac{\partial T}{\partial x} \tag{15}$$

$$\left(\frac{\partial\langle n\rangle}{\partial t}\right)_{\text{decay}} = -\frac{\langle n\rangle - \langle n\rangle^0}{\tau} \tag{16}$$

$$Q_x = \frac{1}{V}\sum_{q,j}\hbar\omega\left(\langle n\rangle - \langle n\rangle^0\right)v_x \tag{17}$$

$$\lambda_L = \frac{1}{3V}\sum_{q,j}v(q,j)\Lambda(q,j)\frac{\partial}{\partial T}\varepsilon(\omega(q,j),T) \tag{18}$$

where $\langle n\rangle$ is the phonon number, v is the energy transport velocity of phonons, τ is a relaxation time approximation, λ_L is the phonon thermal conductivity, Λ is the mean free path for phonon, and $\partial/\partial T\varepsilon$ denotes the heat capacity.

Meanwhile, it is not difficult to notify that TC along the vertical direction is consistent with sintering pressure for the porous anodes. In general, the sintering pressure at properly high levels can easily make big pores collapse into small pores. As a result, TC,
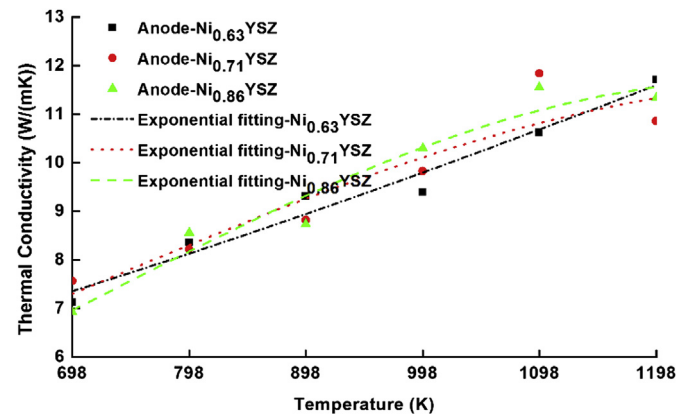

Fig. 4. TC of the porous anodes reconstructed at various Ni contents, 10 bar and 1600 K.

Table 1
The comparison of predicted TC with open literature experimental data.

Ref. [12]	11 W m^{-1} K^{-1}
Ref. [22]	23 W m^{-1} K^{-1}
Ref. [52]	6.23 W m^{-1} K^{-1}
Current work	2–13 W m^{-1} K^{-1}

mechanical strength and TPB's length in the high-pressure sintered anodes are benefited simultaneously.

In Fig. 4, the effect of Ni content on TC in the anode is taken into account. The change of TC in horizontal direction is similar to Fig. 3. Vertically, the square-symbolized curve represents the case with the lowest Ni content, and it is found that phonon heat conduction is dominating in the corresponding anode due to relatively abundant YSZ phase. In contrast, the heat energy is mainly carried by free electrons from the Ni phase in both other cases, which indicates that TC tends to flatten with increasing temperature.

In both figures, the quantities of TC are in good agreement with the open literature data [12,22,52], as shown in Table 1.

Based on Table 1, the simulation results are validated against experimental data, and presented here to give a detailed insight about anodic TC. It is found that a TC range from 2 to 13 W m^{-1} K^{-1} for the porous anodes is relatively reliable, and the difference can be explained by various compositions and sintering conditions applied, as discussed above.

3.3. Thermal expansion

In physics, thermal expansion describes a tendency of materials to change in volume in response to a temperature change, which always takes place when a substance is heated or cooled due to the particles moving, denoted by a temperature-dependent variable, the so-called TEC.

$$\alpha_V = \frac{1}{V} \left(\frac{\partial V}{\partial T} \right)_p \tag{19}$$

Accurate estimation of thermal expansion in the cermet-based anode is a key concern for a wide range of reasons, and it is evidenced that the importance of thermal expansion in the porous anode cannot be over-emphasized by massively extensive research work. Otherwise, the cermet-based anode is apt to crack because YSZ is brittle and cannot tolerate a sudden temperature change. Consequently, the Ni phase and the YSZ phase have to work well in consort and their thermal expansion must be matched in the
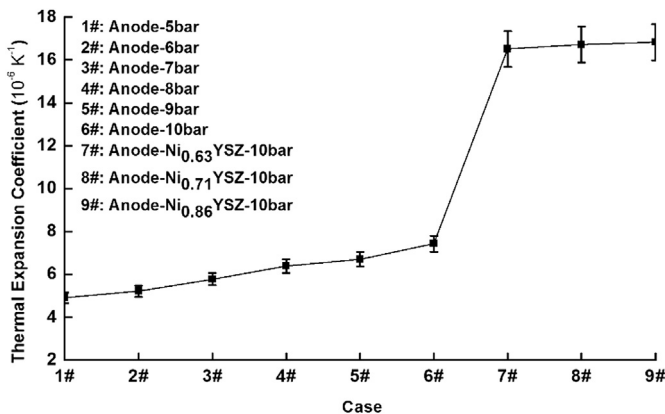
application at a wide range from room temperature to 1200 K. As a remarkable advantage of sintering, the thermal expansion of the NiO and YSZ species can be controlled by firing to generate crystalline distributions that will influence the overall expansion of the resulting material in the desired direction. In addition, a comprehensive trade-off must be done with an eye on other properties affected, e.g., density, porosity, tortuosity, robustness, etc. In this section, TEC is calculated for the porous anodes, which are sintered at diverse conditions as previously described.

Fig. 5 shows the average TEC of the porous anodes, which are reconstructed at different sintering pressures and Ni contents in MD technique. Cases 1–6 illustrate that the sintering pressure has a slight effect on the resulting TEC. This means TEC of the porous anodes with a composition of Ni$_{0.33}$YSZ is in a weakly positive correlation with the sintering pressure. In theory, thermal expansion generally decreases with increasing bond energy, at the same time, the bond energy has a negative tendency with increasing external pressure. In addition, the Ni phase usually represents higher thermal expansion in volume, typically 39E-6 K^{-1} [53,54] compared to the YSZ phase at 10.6E-6 K^{-1} roughly. As a result, thermal expansion of the anodes tends to be worse if higher Ni contents are attempted. According to the open literature data, a combined value of around 12.5E-6 K^{-1} [55] is tolerated in practical applications, which corresponds to the ones with the low Ni content (cases 1–6 in Fig. 5). However, it is still poorly understood how to match thermal expansions caused by Ni and YSZ phases to a good balance.

3.4. Volumetric heat capacity

In the process of heat transfer, VHC is often used to measure how much internal energy (totally including kinetic energy and potential energy) could be stored in a given volume of a substance when undergoing a given temperature change without phase-change.

$$C_V = \frac{1}{V} \frac{\Delta Q}{\Delta T} \tag{20}$$

Approximately, for a given composite, like Ni/YSZ involved in this work, the VHC is directly proportional to the density and SHC of these materials. At the same time, there exists a noticeable positive correlation between sintering pressure and the densities of the sintered anodes. In heat transfer, a higher value of the VHC means longer time for the system to reach equilibration. In other words, the big VHC (in proportion to the density of the resulting material) is desired because it corresponds to a time period required for a change in temperature occurring in the porous anode.
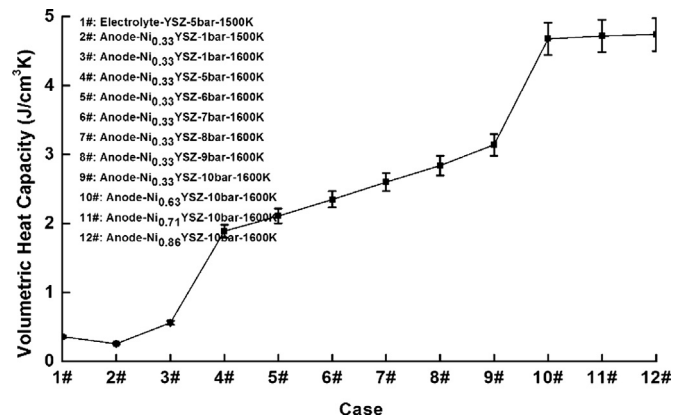

Fig. 5. TEC of the porous anodes reconstructed at various pressures, Ni contents and 1600 K.

Fig. 6. VHC of the porous anode sintered at various pressures and compositions.

Fig. 6 illustrates that the predicted VHC is in positive correlation to sintering pressure and Ni content. In principle, the VHC corresponding to a given porous anode is subject to the molar mass, volume, bulk density and the number of involved atoms, in terms of the Dulong−Petit law [56] as shown in Equations (21) and (22).

$$CM = 3R \tag{21}$$

$$C_V = C\rho = \frac{3R\rho}{M} = \frac{3k_BN}{V} \tag{22}$$

where C is specific heat capacity (J kg^{-1} K^{-1}), M is the molar mass (g mol^{-1}), C_V is volumetric heat capacity (J cm^{-3} K^{-1}), ρ is bulk density (g cm^{-3}), k_B is Boltzmann constant, N is the total number of atoms involved in the system, and R is the gas constant (J K^{-1} mol^{-1}).

It is clearly noticed in Fig. 6 that, to the cermet with a specific composition, the increased VHC is due to the system densification with increasing sintering pressure (cases 2−9). In addition, at the constant system volume, the VHC increases with increasing the number of Ni atoms, i.e., increasing Ni content (cases 9−12).

The predicted values of VHC in Fig. 6 are comparable to the open literature data [52,57,58] as shown in Table 2. In Ref. [52], an experimental value of 1.49 was reported when the anode with 30% porosity was employed. A difference compared to this work can be explained by the distinct anodic compositions. Yang et al., indicated a value of 1.35 in their research work [57]. In Ref. [58], the effect of yttria content on the VHC of YSZ was measured experimentally. One found that the VHC of YSZ decreases with increasing yttria content. In general, the VHC is dependent on the anodic composition, as well as Ni content and sintering pressure. Unfortunately, it is a bit difficult to justify all numerical values due to insufficient experimental data. However, the approaches applied in this study have been validated, and it would be reasonable to mimic the sintering process and predict relevant thermal properties.

3.5. Size effect on thermal conductivity

A lot of investigations for SOFC at the nanoscale have been conducted during past years, which are attempted to exploit the inspiring performance for SOFC as deep as possible. At the same time, the advent of the micro revolution also requires that the physical properties of involved materials must be properly estimated, which in particular requires a suitable size of the simulation domain. The effect of the simulation domain size on the TC should be taken into account in the thermal design for SOFC components. In this study, the bulk material TC is predicted in the porous anode sintered at 8 bar and 1600 K by using a GK method in MD simulations. It is found that a size-independent TC can be achieved with the box size no larger than 200 nm for the high temperature case (1198 K in Fig. 7).

In Fig. 7, it is illustrated that predicted TC of the porous anode is becoming varied with increasing size of the simulation box. When the box size is larger than 200 nm, the TC starts to increase more or less. In addition, the TC of the porous anode in Fig. 7 presents a slight vibration relating to measuring temperatures. Something will account for this phenomenon that in phonon engineering, TC is
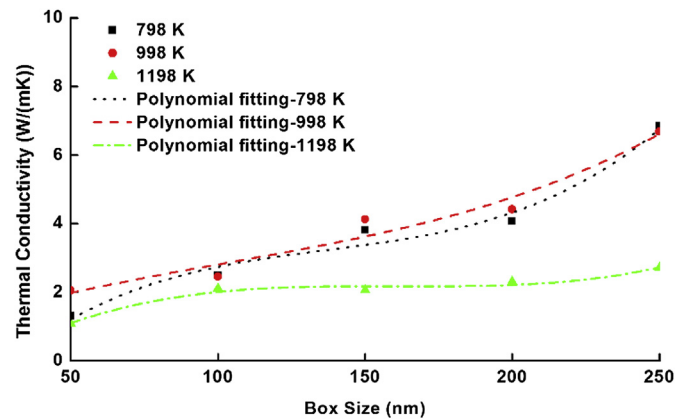
Table 2
The comparison of predicted VHC with the open literature data.

Ref. [52]	1.49 J cm^{-3} K^{-1}
Ref. [57]	1.35 J cm^{-3} K^{-1}
Ref. [58]	2.46−3.85 J cm^{-3} K^{-1}
Current work	0.4−5 J cm^{-3} K^{-1}

Fig. 7. Size effect on TC of the porous anode rebuilt at 8 bar and 1600 K.

related to a temperature-dependent parameter, i.e., mean free path of phonon as shown in Equation (23).

$$k = \frac{1}{3}C_V\bar{v}l \tag{23}$$

where $\bar{v}$ is the phononic velocity (m s^{-1}), l is mean free path of phonon (m).

According to another research work [21], it is described that the extrapolation for the bulk TC is relatively reliable when the system size used in the MD simulations is comparable to the largest mean free path of phonons, which can be determined according to Equation (24).

$$l = \frac{k_BT}{\sqrt{2}\pi d^2 p} \tag{24}$$

where k_B is the Boltzmann constant in J K^{-1}, T is the temperature in K, p is pressure in Pa, and d is the diameter of the involved particles in m.

4. Conclusions

With development in sciences and technologies, a rather big amount of investigations for SOFC at the nanoscale are appearing. On the basis of this background, the microscopic structures of the porous anode of SOFC are reconstructed, and then its thermal properties are systematically calculated based on the molecular dynamics simulations. In this study, the all-atom coarse-grained molecular dynamics method is developed, which contributes to the above numerical computations. In general, when the nano-sintering technology is applied in practice to pursue the good performance of the porous anode relevant to the well-balance of continuity, dispersity, conductivity, porosity and tortuosity, the key point is how to control the sintering pressure and temperature, particle size and composition. Compared to the conventional fabrication process, the nano-sintering technology can produce the well-distributed nanostructure, and a phenomenon of phase aggregation is also avoided successfully. Thermal conductivity is in positive correlation to the sintering pressure, and in low Ni anodes, it slightly increases with measuring temperature due to phonon heat conduction. Instead, in rich Ni anodes, this tendency is flattening owing to heat conduction contributed by free electrons. Thermal expansion increases with increasing sintering pressure and Ni content due to increasing bond energy. The increased VHC is due to the system densification with increasing sintering pressure. In addition, at the constant system volume, the VHC increases with

increasing Ni content. The effect of the simulation domain size on thermal conductivity is also evaluated. It shows that the extrapolation for the bulk thermal conductivity is reliable when the box size is comparable to the biggest mean free path of phonons involved in the simulation system, otherwise, an oscillation is presented. Meanwhile, the simulation results are compared against experimental data, with reasonable agreement. It is believed that a successful thermal design for the porous anode represents a comprehensive balance for its sintering pressure, temperature, as well as particle size and species composition in the fabrication process.

Acknowledgments

References

[1] B. Delhomme, A. Lanzini, G.A. Ortigoza-Villalba, S. Nachev, P. de Rango, M. Santarelli, P. Marty, P. Leone, Int. J. Hydrogen Energy 38 (2013) 4740–4747.
[2] X.-J. Wu, X.-J. Zhu, Int. J. Energy Res. 37 (2013) 242–249.
[3] L. Fan, Z. Qu, M.J.B.M. Pourquie, A.H.M. Verkooijen, P.V. Aravind, Fuel Cells (2013) 1–18.
[4] J.G. Speight, in: D. Shekhawat, J.J. Spivey, D.A. Berry (Eds.), Fuel Cells: Technologies for Fuel Processing, Elsevier, Amsterdam, 2011, pp. 29–48.
[5] W. He, J. Zou, B. Wang, S. Vilayurganapathy, M. Zhou, X. Lin, K.H.L. Zhang, J. Lin, P. Xu, J.H. Dickerson, J. Power Sources 237 (2013) 64–73.
[6] J. Yu, Shanghai Jiao Tong University, 2012.
[7] J.S. Cronin, Y.-C.K. Chen-Wiegart, J. Wang, S.A. Barnett, J. Power Sources 233 (2013) 174–179.
[8] K. Yakal-Kremski, J.S. Cronin, Y.-C.K. Chen-Wiegart, J. Wang, S.A. Barnett, Fuel Cells (2013) 1–6.
[9] A. Predith, G. Ceder, C. Wolverton, K. Persson, T. Mueller, Phys. Rev. B 77 (2008), 144104.144101–144104.144107.
[10] J.C. Ray, R.K. Pati, P. Pramanik, J. Eur. Ceram. Soc. 20 (2000) 1289–1295.
[11] J. Zhou, C.-A. Wang, J. Am. Ceram. Soc. 96 (2013) 266–271.
[12] S. Amiri, R.E. Hayes, K. Nandakumar, P. Sarkar, J. Power Sources 233 (2013) 190–201.
[13] V. Lawlor, J. Power Sources 240 (2013) 421–441.
[14] J. Li, W. Kong, Z. Lin, J. Power Sources 232 (2013) 106–122.
[15] R. Quey, H. Suhonen, J. Laurencin, P. Cloetens, P. Bleuet, Mater. Charact. 78 (2013) 87–95.
[16] Y. Zhang, Q. Sun, C. Xia, M. Ni, J. Electrochem. Soc. 160 (2013) F278–F289.
[17] J. Yang, H. Muroyama, T. Matsui, K. Eguchi, J. Power Sources 236 (2013) 192–199.
[18] J. Im, I. Park, D. Shin, Ceram. Int. (2013).
[19] S. Nichenko, D. Staicu, J. Nucl. Mater. 439 (2013) 93–98.
[20] Q. Jeangros, A. Faes, J.B. Wagner, T.W. Hansen, U. Aschauer, J. Van herle, A. Hessler-Wyser, R.E. Dunin-Borkowski, Acta Mater. 58 (2010) 4578–4589.
[21] D.P. Sellan, E.S. Landry, J.E. Turney, A.J.H. McGaughey, C.H. Amon, Phys. Rev. B 81 (2010), 214305.214301–214305.214310.
[22] S.A. Tabei, A. Sheidaei, M. Baniassadi, F. Pourboghrat, H. Garmestani, J. Power Sources 235 (2013) 74–80.
[23] M.C. Williams, in: S. Dushyant, J.J. Spivey, A.B. David (Eds.), Fuel Cells, Elsevier, Amsterdam, 2011, pp. 11–27.
[24] S. Kakac, A. Pramuanjaroenkij, X.Y. Zhou, Int. J. Hydrogen Energy 32 (2007) 761–786.
[25] Y. Guan, W. Li, Y. Gong, G. Liu, X. Zhang, J. Chen, J. Gelb, W. Yun, Y. Xiong, Y. Tian, H. Wang, J. Power Sources 196 (2011) 1915–1919.
[26] K.N. Grew, W.K. Chiu, J. Power Sources 199 (2012) 1–13.
[27] P. Souvatzis, A. Niklasson, Chem. Phys. (2013).
[28] D.J. Diestler, A. Kenfack, J. Manz, B. Paulus, J.F. Perez-Torres, V. Pohl, J. Phys. Chem. A (2013).
[29] J.K. Seo, A. Khetan, M.H. Seo, H. Kim, B. Han, J. Power Sources 238 (2013) 137–143.
[30] J.B. Accary, V. Teboul, J. Chem. Phys. 136 (2012), 094502.094501–094502.094507.
[31] K.T. Lee, A.A. Lidie, S.Y. Jeon, G.T. Hitz, S.J. Song, E.D. Wachsman, J. Mater. Chem. A 1 (2013) 6199–6207.
[32] K.C. Lau, B.I. Dunlap, J. Phys. Condens. Matter 23 (2011), 035401.035401–035401.035416.
[33] T. Sasaki, K. Matsunaga, H. Ohta, H. Hosono, T. Yamamoto, Y. Ikuhara, Mater. Trans. 45 (2004) 2137–2143.
[34] B. Bayramoglu, R. Faller, Macromolecules 45 (2012) 9205–9219.
[35] Y. Xiao, J. Yuan, B. Sundén, J. Electrochem. Soc. 159 (2012) B251–B258.
[36] S.J. Marrink, H.J. Risselada, S. Yefimov, D.P. Tieleman, A.H. De Vries, J. Phys. Chem. B 111 (2007) 7812–7824.
[37] S. Pronk, S. Páll, R. Schulz, P. Larsson, P. Bjelkmar, R. Apostolov, M.R. Shirts, J.C. Smith, P.M. Kasson, D. Van der Spoel, B. Hess, E. Lindahl, Bioinformatics (2013) 1–10.
[38] B. Hess, C. Kutzner, D. Van der Spoel, E. Lindahl, J. Chem. Theory Comput. 4 (2008) 435–447.
[39] I.G. Tejada, R. Jimenez, Eng. Comput. 30 (2013) 301–316.
[40] C.F. Schwenk, H.H. Loeffler, B.M. Rode, J. Chem. Phys. 115 (2001) 10808.
[41] N. Kurita, H. Inoue, H. Sekino, Chem. Phys. Lett. 370 (2003) 161–169.
[42] A. Hauch, P.S. Jørgensen, K. Brodersen, M. Mogensen, J. Power Sources 196 (2011) 8931–8941.
[43] A.C. Müller, D. Herbstritt, E. Ivers-Tiffée, Solid State Ionics 152–153 (2002) 537–542.
[44] M.H.D. Othman, N. Droushiotis, Z. Wu, G. Kelsall, K. Li, J. Power Sources 205 (2012) 272–280.
[45] Y.J. Leng, S.H. Chan, K.A. Khor, S.P. Jiang, P. Cheang, J. Power Sources 117 (2003) 26–34.
[46] J. Kim, K.H. Cho, I. Kagomiya, K. Park, Ceram. Int. (2013).
[47] W. Kong, H. Zhu, Z. Fei, Z. Lin, J. Power Sources 206 (2012) 171–178.
[48] S. Nichenko, D. Staicu, J. Nucl. Mater. 433 (2012) 297–304.
[49] W.F. Goh, T.L. Yoon, S.A. Khan, Comput. Mater. Sci. 60 (2012) 123–129.
[50] A. Paussa, D. Esseni, J. Appl. Phys. 113 (2013), 093702.093701–093702.093713.
[51] J.M. Loy, J.Y. Murthy, D. Singh, J. Heat Transfer 135 (2013), 011008.011001–011008.011012.
[52] M. Liu, M.J.B.M. Pourquie, L. Fan, W. Halliop, V.R.M. Cobas, A.H.M. Verkooijen, P.V. Aravind, Fuel Cells (2013).
[53] D.A. Burdin, Y.K. Fetisov, D.V. Chashin, N.A. Ekonomov, Tech. Phys. 58 (2013) 414–419.
[54] C.E. Whiteley, M.J. Kirkham, J.H. Edgar, J. Phys. Chem. Solids 74 (2013) 673–676.
[55] S.K. Pratihar, A. Das Sharma, R.N. Basu, H.S. Maiti, J. Power Sources 129 (2004) 138–142.
[56] H. Wang, W.D. Porter, H. Böttner, J. König, L. Chen, S. Bai, T.M. Tritt, A. Mayolet, J. Senawiratne, C. Smith, F. Harris, P. Gilbert, J. Sharp, J. Lo, H. Kleinke, L. Kiss, J. Electron. Mater. 42 (2013) 1073–1084.
[57] C. Yang, G. Yang, D. Yue, J. Yuan, B. Sunden, J. Renew. Sustain. Energy 5 (2013), 021420.021421–021420.021418.
[58] X. Song, M. Xie, F. Zhou, G. Jia, X. Hao, S. An, J. Rare Earths 29 (2011) 155–159.